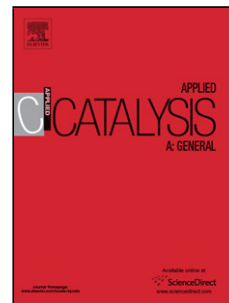


Journal Pre-proof

Exploring the multifunctionality and accessibility of vanadosilicates to produce acrylic acid in one-pot glycerol oxydehydration

Luiz H. Vieira (Conceptualization) (Investigation) (Formal analysis) (Writing - original draft), Alejandro Lopez-Castillo (Software) (Resources) (Writing - review and editing), Christopher W. Jones (Supervision) (Resources) (Writing - review and editing), Leandro Martins (Conceptualization) (Funding acquisition) (Supervision) (Writing - review and editing)



PII: S0926-860X(20)30280-5
DOI: <https://doi.org/10.1016/j.apcata.2020.117687>
Reference: APCATA 117687

To appear in: *Applied Catalysis A, General*

Received Date: 30 March 2020
Revised Date: 16 May 2020
Accepted Date: 1 June 2020

Please cite this article as: Vieira LH, Lopez-Castillo A, Jones CW, Martins L, Exploring the multifunctionality and accessibility of vanadosilicates to produce acrylic acid in one-pot glycerol oxydehydration, *Applied Catalysis A, General* (2020), doi: <https://doi.org/10.1016/j.apcata.2020.117687>

This is a PDF file of an article that has undergone enhancements after acceptance, such as the addition of a cover page and metadata, and formatting for readability, but it is not yet the definitive version of record. This version will undergo additional copyediting, typesetting and review before it is published in its final form, but we are providing this version to give early visibility of the article. Please note that, during the production process, errors may be discovered which could affect the content, and all legal disclaimers that apply to the journal pertain.

© 2020 Published by Elsevier.

Exploring the multifunctionality and accessibility of vanadosilicates to produce acrylic acid in one-pot glycerol oxydehydration

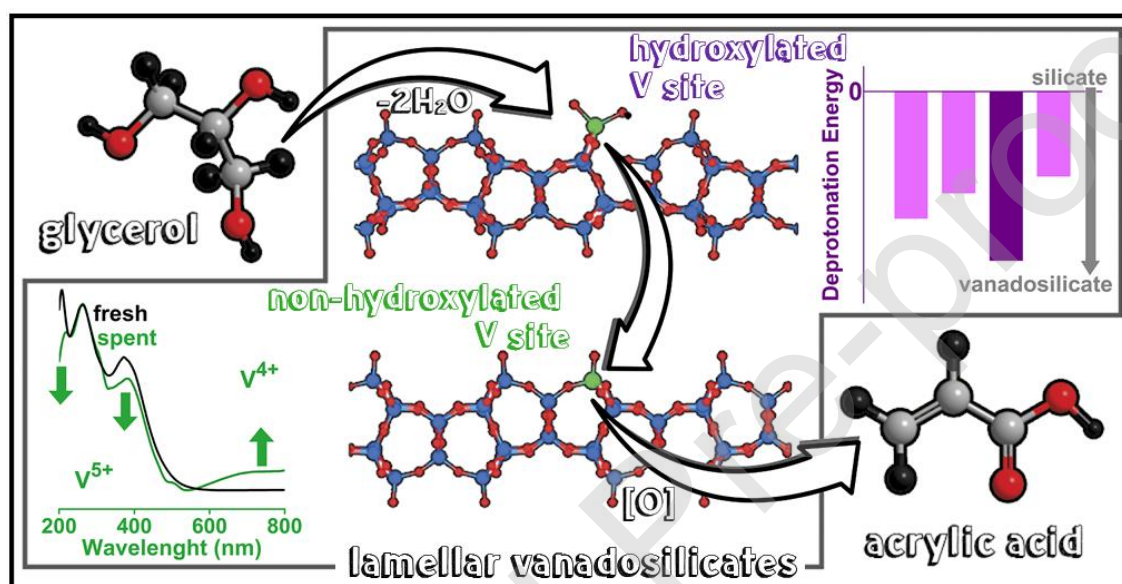
Luiz H. Vieira^{1,2}, Alejandro Lopez-Castillo³, Christopher W. Jones², Leandro Martins^{*1}

¹ Institute of Chemistry, São Paulo State University - UNESP, R. Prof. Francisco Degni 55, Araraquara, SP, 14800-900, Brazil

² School of Chemical & Biomolecular Engineering, Georgia Institute of Technology, Atlanta, GA, 30332-0100, United States

³ Department of Chemistry, Federal University of São Carlos, Rod. Washington Luís, km 235, 13565-905, São Carlos, SP, Brazil

Graphical Abstract



Highlights

- ✓ Preparation of Al-free vanadosilicates presenting 2D and 3D structures
- ✓ Productivity of acrylic acid was improved on delaminated ITQ-6
- ✓ Brønsted acid sites were formed due to dissociative adsorption of water
- ✓ DFT calculations: deprotonation energy of Brønsted acidic sites of vanadosilicates

Abstract

Acrylic acid is one of the most attractive products directly produced from glycerol, and many efforts are still made to thoroughly understand the role of different catalytic sites in the reaction. In this work, we prepared Al-free vanadosilicates presenting structures analog to ferrierite and ITQ-6 zeolites (2D and 3D structures). The materials were efficient in catalyzing the one-pot conversion of glycerol to acrylic acid. The different vanadium species in the catalysts had specific roles in each step of the reaction. By exposing samples to humid conditions, dissociative adsorption of water produced hydroxylated sites ($\text{O}_3\text{V-OH-Si}$) that acted as extrinsic Brønsted acid sites. The deprotonation energy of these sites was estimated by DFT calculations and found to be close to deprotonation energy of intrinsic Brønsted acidity of aluminosilicates with the same zeolitic structure, indicating the ability of the active site to dehydrate glycerol to acrolein. The formation of these sites seems to effectively block potential Lewis acidity of the vanadosilicates since acetol, a dehydration side product, was not formed. Spectroscopic data showed changes in oxidation states of vanadium in these sites after the reaction, presenting V^{5+} and V^{4+} states, indicating the activity of these sites on the oxidation step during oxidation of acrolein to acrylic acid. By decreasing vanadium content during synthesis, delamination to ITQ-6 was more effective, increasing accessibility and, consequently, the productivity of sites.

Keywords: acrylic acid; ferrierite; ITQ-6; vanadium; dehydration; oxidation.

INTRODUCTION

The limited supply of fossil fuels and climate change policies have driven the development and application of renewable carbon source routes for energy generation.[1] Biofuels are emerging in this scenario, and during the last decades, they have been even further researched and produced. Notably, biodiesel arose as a substitute for fossil-derived diesel, presenting comparable properties. Its production is based on transesterification of vegetable oils from various sources and generates large amounts of glycerol as a by-product.[2] Oversupply and the consequent drop in prices placed the focus on glycerol research to produce chemicals, polymers, and fuels.[3] Glycerol upgrading is a promising way to equate profits of biodiesel and conventional diesel, increasing competitiveness and, perhaps, leading to the ideal point of complete transition from the refinery to the biorefinery.

The production of acrylic acid from glycerol is a route that can be performed in a single reactor. The significance of the process relies on the uses of the simplest unsaturated carboxylic acid, which is a chemical intermediate for the polymer industry with a market size comparable to glycerol availability (around 6 Mt.y⁻¹) and a high price (around 1.6-1.8 USD.kg⁻¹).[3,4] It can be produced using various intermediates derived from glycerol as acrolein[5], allyl alcohol[6], lactic acid[7], and acrylonitrile[8], but oxidative dehydration is a short method to produce acrylic acid from glycerol[9]. Two steps are required to conduct this reaction: (1) dehydration of glycerol to acrolein by protonation of the secondary hydroxyl group and subsequent (2) oxidation of acrolein to acrylic acid.[10] The oxidation step is well known and established since it is industrially applied in acrylic acid production from fossil-derived propylene.[11] In this process, molybdenum-vanadium[12], cobalt-molybdenum[13], and vanadium-antimony[14] are often applied in the oxidation of acrolein *via* Mars-van Krevelen mechanism[15], presenting high conversions and acrylic acid as a primary product. Mostly, the dehydration step is conducted by applying materials presenting acid sites, and it

was established that the formation of acrolein is associated with Brønsted acid sites. In contrast, Lewis acid sites promote the formation of acetol (Figure S1) [16]. Catalysts employed for this reaction generally comprise strong Brønsted site materials, like heteropolyacids [17] and zeolites [18], presenting satisfactory activities but suffering from rapid deactivation. The use of weak solid acids likes, Al-free Ga-zeolites [19], and iron phosphates [20], or co-feeding of oxygen during reaction [21] were found to be effective strategies to avoid deactivation by coke, increasing the stability of the catalysts.

To directly convert glycerol into acrylic acid by oxidative dehydration in a single-bed reactor, the development of catalysts is focused on combining elements that bring intrinsic Brønsted acidity and oxidant properties to the material. MoVWO mixed oxides [22], VO/zeolites [23], and MoVO/heteropolyacids [24] are commonly applied as catalysts, combining acidity and the oxidant property of vanadium. Despite being potential Lewis acids, it is common to use some transition metals in dehydration reactions [25] since they can accept electrons on vacant *d* orbitals. Recent studies identified extrinsic Brønsted acidity over niobium [16] and vanadium [26] active sites generated by dissociative adsorption of water. The strong intermolecular interactions present in glycerol make it challenging to run in gas-phase processes since glycerol starts to decompose, forming unwanted compounds at temperatures close to its boiling point [27]. In this way, most of the processes involving continuous feeding of glycerol are based on aqueous solutions. Notably, the need for water in the process may be advantageous for adding functionality to the vanadium catalytic sites for the dehydration to acrolein.

Herein, we report the preparation of 3D and 2D Al-free lamellar vanadosilicates, with structures analogous to ferrierite and ITQ-6 zeolites. We found that these materials possess high activity to directly produce acrylic acid from glycerol, even in the absence of framework aluminum, which provides intrinsic Brønsted acidity. Both catalysts were prepared via

treatments of the lamellar precursor, called [V]-PreFER(25). The number in parenthesis in nomenclature refers to the Si/V ratio in the synthesis mixture that was fixed at 25, and 2,2,6,6-tetramethylpiperidine was applied as a structure-directing agent (SDA). The 3D [V]-FER(25) catalyst was prepared by direct calcination of [V]-PreFER(25) and 2D [V]-ITQ-6(25) prepared by the expansion of layers of the precursor by adding hexadecyltrimethylammonium bromide (CTABr) followed by delamination. The structures of the materials were mainly investigated by X-ray diffraction (XRD), N₂ physisorption, transmission electron microscopy (TEM) and Fourier-transform infrared spectroscopy (FTIR), the nature of vanadium sites on catalysts were investigated by UV-vis spectroscopy, acidity was estimated by density functional theory (DFT) calculations of deprotonation energies of vanadosilicates and compared to that calculated for Brønsted acid sites of aluminosilicates in the same structure.

EXPERIMENTAL SECTION

Synthesis of the lamellar precursor. For the synthesis of [V]-PreFER, an aqueous solution of vanadyl oxide sulfate (hydrate, 97%, Sigma-Aldrich) and ammonium fluoride (≥98%, Sigma-Aldrich) was prepared, then the 4-amino-2,2,6,6-tetramethylpiperidine (98%, Sigma-Aldrich) was dropwise added. In the last step, fumed silica (powder, 200-300 nm avg. part. size, Sigma-Aldrich) was added slowly, and the solution remained under vigorous stirring for 3 h. Thermal treatment was performed in a stainless-steel autoclave at 150 °C for 120 h. The crystalline product obtained was filtered and washed with an acetic acid aqueous solution and distilled water until getting a pH < 9. The following molar composition of reactants was used: 1 SiO₂: 0.067 VO₂SO₄: 2 NH₄F: 1 R: 10 H₂O. The material was called [V]-PreFER(25) since the Si/V ratio of the synthesis mixture was 25. Two additional precursors were synthesized, comprising Si/V ratios of 15 and 40, and were called [V]-PreFER(15) and [V]-PreFER(40), respectively.

Preparation of 3D and 2D vanadosilicates. For the preparation of 3D [V]-FER catalyst, the lamellar precursor [V]-PreFER was calcined at 620°C (rate of 5°C.min⁻¹) for 6 h in air. After thermal treatment, the catalyst was washed with an acetic acid aqueous solution and distilled water. For the preparation of 2D [V]-ITQ-6, layers of precursor [V]-PreFER (~10 g) were expanded by treatment in a refluxing aqueous solution (~80 g of H₂O) containing ~50 g of hexadecyltrimethylammonium bromide (CTABr, ≥98%, Sigma-Aldrich) and ~100 g of tetrapropylammonium hydroxide (TPAOH, 1 mol.L⁻¹ in H₂O, Sigma-Aldrich) at 85°C for 22 h. The swollen precursor was remained under an ultrasound bath for 2 h at room temperature to delamination of the structure and added to an aqueous solution of hydrochloric acid (pH of about 2). The solid product was filtered, washed with an acetic acid aqueous solution and distilled water, dried, and calcined at 620°C (rate of 5°C.min⁻¹) for 6 h in air.

Characterization of materials. The vanadium content in the catalysts was determined by Inductively Coupled Plasma-Optical Emission Spectrometry (ICP-OES) of digested samples using an Optima 8000 spectrometer. Acid digestion was performed by suspending 100 mg of sample in 1 mL of distilled water, followed by the addition of 0.1 mL of sulfuric acid (Sigma-Aldrich, nominally 95-98% H₂SO₄) and 1 mL of hydrofluoric acid (Sigma-Aldrich, 48 wt.% in H₂O, purity > 99.9%). The suspension was heated to 100°C during 2 h, and the resulting volume was diluted in 100 mL of deionized water.

X-ray diffraction patterns were obtained at the XPD beamline of the Brazilian Synchrotron Light Laboratory (LNLS). The XPD beamline was equipped with a Huber 4+2 circle diffractometer, and a Eulerian cradle (model 513) positioned ca. 13 m from a double-bounce Si (111) monochromator ($\lambda = 0.1377$ nm). The data were collected in high-resolution mode, employing a Si(111) analyzer crystal and a Mythen detector. The measurements were performed from room temperature to 500 °C at 10°C/min under air, in the 2 θ range from 7 to 40°, with, approximately, 8 min for each acquisition. Structures were refined by the Rietveld

method using TOPAS®4.2 software. The occupancy and temperature factors of all atoms were fixed, and the unit cell parameters, scale factor, and atomic positions (except for special positions: 0, 1/4, 1/3, 1/2 etc.) were refined. Sample displacement, zero error, and intensity corrections were refined as well. The background was fitted using a fifth-order Chebyshev polynomial function. Fundamental parameters profile fitting (FPPF) was used for the peak profile refinements.

Nitrogen physisorption isotherms of vanadium oxide supported catalysts were performed on a Micromeritics Tristar II instrument at liquid nitrogen temperature (-196 °C), with a relative pressure interval of between 1×10^{-3} and 0.998. Before the measurements, the samples were evacuated at 200 °C for 12 h. Micropore volumes of all samples were determined by using the t-plot method. Mesopore volumes were determined by the difference between total pore volume at $P/P_0 = 0.95$ and the micropore volumes. Pore size distributions were determined by applying the Barrett-Joyner-Halenda (BJH) method.

Transmission electron micrograph (TEM) images were obtained on a FEI Tecnai F30 at 300 kV. The samples were suspended in ethanol and dispersed over a holey carbon film grid for subsequent imaging.

Diffuse reflectance UV-vis spectra were obtained in the range from 190 to 800 nm, using a dual-beam Perkin Elmer Lambda 1050 UV/Vis/NIR spectrophotometer equipped with an integrating sphere. The reflectance was converted using the Kubelka-Munk equation and was plotted as a function of the wavelength. In addition to the catalysts, the UV-Vis spectrum of vanadium pentoxide (V_2O_5), prepared from calcination of $VOSO_4$, was recorded for reference.

The solid-state ^{29}Si DP/MAS-NMR spectra were recorded using a Varian INOVA 500 spectrometer equipped with a 4 mm probe, at a spinning rate of 14 kHz applying the following

experimental conditions: operating frequency of 79.49 MHz, acquisition time of 0.8192 ms, pulse width of 3.4 ms, and recycle delay of 700 s.

Temperature programmed desorption of ammonia (TPD-NH₃) profiles were acquired by a continuous flow reaction system coupled to a PrismaPlus QMG 220 (Pfeiffer) mass spectrometer. In a typical experiment, 200 mg of sample was placed in the reactor and kept under a He flow (50 mL.min⁻¹) at 500 °C for 1 h, followed by cooling to 100 °C. At this temperature, the sample was exposed to a flow of 1% NH₃ in He (50 mL.min⁻¹) for 1 h. The excess and physically adsorbed NH₃ were then purged at 100 °C under a flow of He (50 mL.min⁻¹) during 1 h. Finally, NH₃ was desorbed by heating reactor from 100 to 500 °C (10 °C.min⁻¹) in a He flow of 50 mL.min⁻¹.

The chemisorption of pyridine spectra were collected on Shimadzu Prestige IR 21 using a glass transmission cell. Approximately 20 mg of samples were pressed into self-supported wafers, vacuum treated (0.013 Pa) at room temperature to 300 ° C, and held at that temperature for 30 min. The sample was cooled to room temperature, and the background spectrum was collected. After that, 2 µL of pyridine was injected, and after evacuation for 15 min, a spectrum of chemisorbed pyridine at room temperature was acquired.

The surface hydroxyl species were monitored by Fourier-transform infrared (FTIR) collected in a Thermo Scientific Nicolet iS10 equipped with a mercury-cadmium-telluride (MCT) detector. Catalysts were pressed into self-supported wafers, placed into a high-temperature Harrick transmission cell equipped with CaF₂ windows, and pretreated at 400 °C for 30 min under 50 mL.min⁻¹ of N₂. The spectra were collected immediately after pre-treatment.

Thermogravimetric analysis of the spent catalysts was carried out under air (100 mL.min⁻¹) using a Netzsch thermobalance, with heating from 30 to 900 °C at a rate of 10 °C.min⁻¹.

Density functional theory calculations. The calculations were performed considering the density functional theory (DFT) with B3-LYP hybrid functional (Becke's gradient-corrected exchange-correlation in conjunction with the Lee-Yang-Parr correlation functional with three parameters[28]) with SVP atomic basis sets implemented in the TURBOMOLE software package[29,30]. This DFT methodology is similar to that presented in a previously published paper on this related subject [31]. The molecular geometry optimizations were carried out without symmetry restrictions. The optimization convergence criteria considered a change of 10⁻⁶ au in the total energy and 10⁻³ au in the maximum norm of the gradient. The numerical integration for DFT calculation was considered as 10⁻⁷ au in the grid step, which provides sufficient numerical accuracy for energies and geometries.

Starting from a ferrierite cluster with 350 with atomic coordinates taken from the International Zeolite Association website [32], we reduced to 100 atoms containing the main zeolite cavities. Following reductions were made obtaining clusters with 40, 60, and 80 atoms maintaining yet the cavities. The geometry of these small four structures of ferrierite was optimized using DFT/B3-LYP/SVP method. The small clusters suffered considerably asymmetric geometry deformation. We chose the cluster with near to 80 atoms considering the minor cluster with negligible deformation. Substitutions of some Si atoms by Al and V atoms were made and OH⁻ group was also added. After these modifications, the geometry of clusters was optimized following the same procedure. The total electronic energies were computed at the final of the geometry optimization to obtain the relative energies showed in this work. The XYZ coordinates of some representative optimized structures, comprising siliceous ferrierite ([Si]-FER), aluminosilicate with Al substituted on T1 site ([Al]-FER_T1),

vanadosilicate with V substituted on T1 site ([V]-FER_T1) and vanadosilicate after dissociative adsorption of water ([VO1H]-FER_T1) are provided on Tables S1 to S4. Substitutions on T2, T3 and T4 sites followed the same procedures.

Values of deprotonation energy (E_{dp}) were calculated from geometry optimizations of neutral (ZOH) and deprotonated (ZO⁻) FER type zeolitic structures by the following equation:

$$E_{dp} = E_{ZO^-} + E_{H^+} - E_{ZOH} \quad (1)$$

where E_{ZO^-} , E_{H^+} and E_{ZOH} are the electronic energies of deprotonated structure, proton, and neutral structure, respectively. The electronic energy for proton (E_{H^+}) is null. Vanadium was substituted over the four different T sites of structure. For comparison, the deprotonation energy of pure siliceous and Al-containing zeolites of the same structure were calculated.

The energies of dissociative adsorption of water on vanadium sites in FER structures were determined from geometry optimizations of vanadosilicates (VO) and hydroxylated vanadosilicates (VOH) by the following equation:

$$E_{ads(H_2O)} = E_{ZVOH} - E_{ZVO} - E_{H_2O} \quad (2)$$

where E_{ZVOH} , E_{ZVO} and E_{H_2O} are the electronic energies of hydroxylated V-sites structure, V-containing bare structures, and water, respectively.

The energies of vanadium substitution were determined from geometry optimizations of vanadosilicates (ZVO) and silicates (ZSiO) by the following equation:

$$E_{sub} = (E_{ZVO} + E_{Si}) - (E_{ZSiO} + E_V) \quad (3)$$

where E_{ZVO} , E_{ZSiO} , E_V and E_{Si} are the electronic energies of vanadosilicate, silicates, isolated vanadium atom, and isolated silicon atom, respectively.

Catalytic tests. The one-step oxidative dehydration of glycerol was carried out in continuous flow at 290, 320, 350, or 350 °C and atmospheric pressure. In a typical catalytic test, 200 mg of a finely divided powder of the catalyst were deposited on a fixed bed inside the glass reactor without the use of diluent. The reaction temperature was monitored by a thermocouple

kept in contact with the catalytic bed. The sample was first heated to the reaction temperature under 30 mL.min⁻¹ of a mixed flow composed of 80 % N₂ and 20 % O₂ (mol/mol) and kept at this temperature for 30 min. When reaction started, a solution prepared by adding 10 wt.% glycerol (Sigma-Aldrich, 99%) in deionized water was continuously introduced (at 0.05 mL.min⁻¹) to the heated gas line using a syringe pump (KD Scientific). The flow was kept at 30 mL.min⁻¹ during the reaction, and the following compositions of O₂/N₂/H₂O/C₃H₈O₃ (%mol) were used: 7/27/64/2, 17/17/64/2, or 34/0/64/2. The weight hourly space velocity (WHSV) was 3.8 h⁻¹. The effluent products, collected in a gas-liquid separator kept at 1 °C to ensure the condensation of the more volatile compound (acetaldehyde, boiling point of 20 °C), were analyzed using a gas chromatograph (Shimadzu GC-2014) equipped with a capillary column (Rtx-1, 30m, 0.32mm, 1 μm) and a flame ionization detector (FID). Aliquots of products were collected each 1 h from gas-liquid separator during 6 h of reaction. Before each injection, a known mass of *n*-butanol was added as an internal standard to guarantee a quantitative mass balance for condensed products. Selectivity for CO_x compounds was indirectly determined by carbon balance considering the amount of carbon present on feed and condensed products. The analyses were carried out in triplicate, and the retention times were compared to those of authentic compounds. Conversion of glycerol (X_{gly}) and product selectivities (S_{prod}) were calculated following the equations (4) and (5):

$$X_{gly}(\%) = \frac{n_{gly}^{in} - n_{gly}^{out}}{n_{gly}^{in}} \times 100 \quad (4)$$

$$S_{prod}(\%) = \frac{n_{prod}}{n_{gly}^{in} - n_{gly}^{out}} \times \frac{Z_{prod}}{Z_{gly}} \times 100 \quad (5)$$

where, n_{gly}^{in} and n_{gly}^{out} are the molar flows of glycerol in the input and output, respectively; n_{prod} is the molar flow of product; Z_{gly} is the number of carbon atoms on glycerol molecule and Z_{prod} is the number of carbon atoms on the products. The selectivity to CO_x compounds was calculated by a carbon balance considering the mole flow of glycerol fed and the mole

flow of non-converted glycerol and products leaving the reactor since no residual carbon deposits were detected in the spent catalysts.

Journal Pre-proof

RESULTS AND DISCUSSION

The X-ray diffraction (XRD) patterns in Figure 1a revealed the presence of the crystalline structure of the lamellar precursor[33] [V]-PreFER(25). After calcination, the condensation of PreFER layers was confirmed by displacement of (*h*00) diffraction planes to higher 2θ values (most evident is the (200) plane), which means a decrease in spacing between the 2D layers.[33] Removing the structure-directing agent (SDA) by calcination generates a purely microporous 3D vanadosilicate, as observed by the profile of the physisorption isotherms (Figure 1b), with a micropore volume of approximately $0.1 \text{ cm}^3.\text{g}^{-1}$ (Table S5). Transmission electron microscopy (TEM) images (Figure 1d) show the presence of dense crystals on [V]-FER(25) formed by stacked 2D layers. The interlayer spaces are a result of 8 and 10-membered ring formation [34], with an average distance measured by TEM of around 0.55 nm, which is in line with the calculated spacing from crystallographic information obtained by a structural refinement of the XRD patterns (Figure S2). The expansion of lamellar precursor layers followed by exfoliation generated the sample [V]-ITQ-6(25), composed by disorganized 2D layers[35]. This process avoids the condensation of T2 sites to form 8 and 10-membered rings, exposing terminal positions and generating a highly hydroxylated surface (Figure S3). Structural disorganization suppressed diffraction peaks, resulting in an amorphous profile in the XRD pattern. A physisorption isotherm that combines profiles of microporous and mesoporous materials[36] is observed for this material (Figure 1b), presenting a mesopore volume of $1.2 \text{ cm}^3.\text{g}^{-1}$ and a residual micropore volume of $0.03 \text{ cm}^3.\text{g}^{-1}$ (Table S5), probably associated with some remaining stacked layers and microporosity of individual layers. Generation of a narrow distribution of mesopore diameters around 3 nm (1) and a broad distribution centered around 10 nm (2) are noted in Figure 1c. The group of mesopores presenting smaller diameters is generated by agglomerates of

disorganized layers, while higher diameters are associated with the spaces between these agglomerates, as revealed in TEM images (Figure 1d).

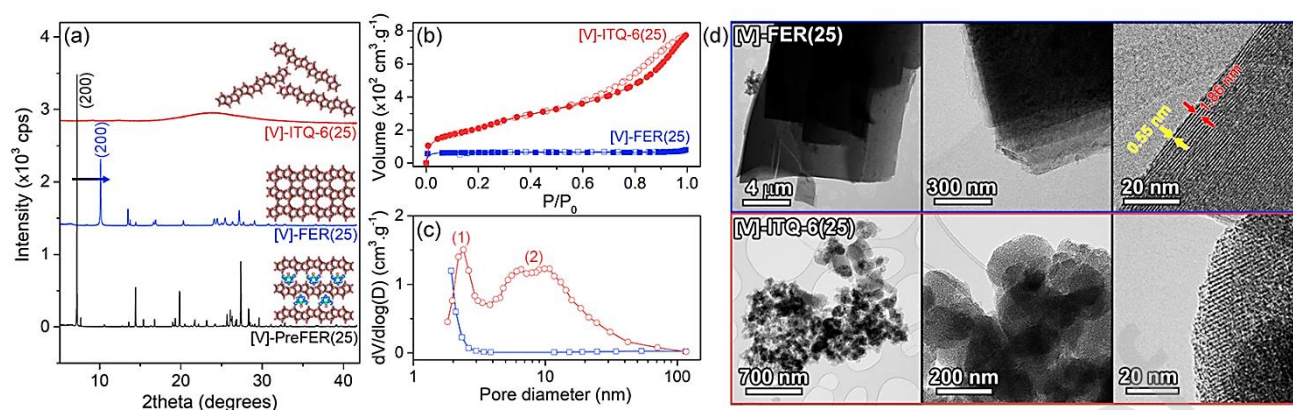


Figure 1. (a) X-ray diffraction patterns of lamellar precursor [V]-PreFER(25), 3D material [V]-FER(25) and 2D material [V]-ITQ-6(25). (b) N₂ physisorption isotherms, (c) pore size distribution and (d) transmission electron microscopy (TEM) images of [V]-FER(25) and [V]-ITQ-6(25).

The incorporation of vanadium in the lamellar precursor was around 31 % (Table S5). This limitation is predicted by Pauling chemical bond theory, where the ratio of metallic cation radius and oxygen anion radius must be in the range 0.225-0.414 for incorporation in the zeolite tetrahedral position [25]. In our synthesis, the mixture was kept in a pH range of 10-11 to guarantee that most of the vanadium was in the form of $\text{VO}_3(\text{OH})^-$ [37], where V is present in 5+ oxidation state, the lowest cation radius among possible V oxidation states. Even V^{5+} will result in a radius ratio of 0.539, out of the Pauling criterion, which justifies the low incorporation. Incorporation of cations that exceed this range is commonly reported in the literature for Ge [38], Sn [39], and Ti [40] atoms. After calcination to produce condensed 3D FER and the delamination process to produce 2D ITQ-6, part of vanadium migrated to extra-framework positions and was subsequently removed via an acetic acid treatment, which further reduced the amount incorporated in these materials (Table S5).

Nature and oxidation states of the vanadium in the materials were investigated by UV-vis spectroscopy. Bands on the spectra are related to charge transfers (CT) of oxygen to vanadium and between vanadium *d* orbitals. The position of the bands (wavelength of CT) is

sensitive to changes in the coordination and oxidation state of vanadium [41]. In Figure 2a, spectra of the as-prepared lamellar precursor and catalysts are shown, indicating the presence of four different bands related to vanadium sites. Bands centered around 220, 260, and 325 nm are observed in the [V]-PreFER(25) precursor and around 220, 260, and 370 nm in [V]-FER(25) and [V]-ITQ-6(25) catalysts. It is generally accepted that bands in the range 200-400 nm are related to V^{5+} species and in the range 600-800 nm to V^{4+}/V^{3+} species [41,42]. Bands around 210 and 260 nm are related to distorted tetrahedral framework sites, where distortion decreases by shifting to higher wavelengths [43-45]. Typically, a more distorted structure (210 nm) is associated with the presence of three Si-O-V bonds and one V=O bond, while less distorted (260 nm) species are related to a tetrahedron containing two Si-O-V bonds, one V=O and a terminal V-O-H group. The band at 325 nm in [V]-PreFER(25) is also assigned to tetrahedral vanadium, but related with the presence of counterion on structure [44,46], since the material was not calcined. This is confirmed by the disappearance of this band in [V]-FER(25) and [V]-ITQ-6(25) catalysts. No bands related to oligomeric species or reduced forms (V^{4+}/V^{3+}) are identified on the precursor since the pH of synthesis mixture was kept around 10-11, which ensures the presence of almost all vanadium species in the solution are isolated $VO_3(OH)^{2-}$ anions. The appearance of a new broad band at 380 nm on FER and ITQ-6 materials suggests the formation of oligomeric sites that can be in both tetrahedral and octahedral coordination in the framework [47]. This is a result of treatments of the precursor due to the aggressive pH of the medium during delamination as well as the high temperature of calcination to prepare the catalysts. The bands in 210 and 260 nm are still present in these materials, indicating a considerable presence of monomeric hydroxylated and non-hydroxylated tetrahedral sites. No bands related to V^{5+} on extra-framework V_2O_5 clusters (Figure S4) were observed after calcination of the precursor.

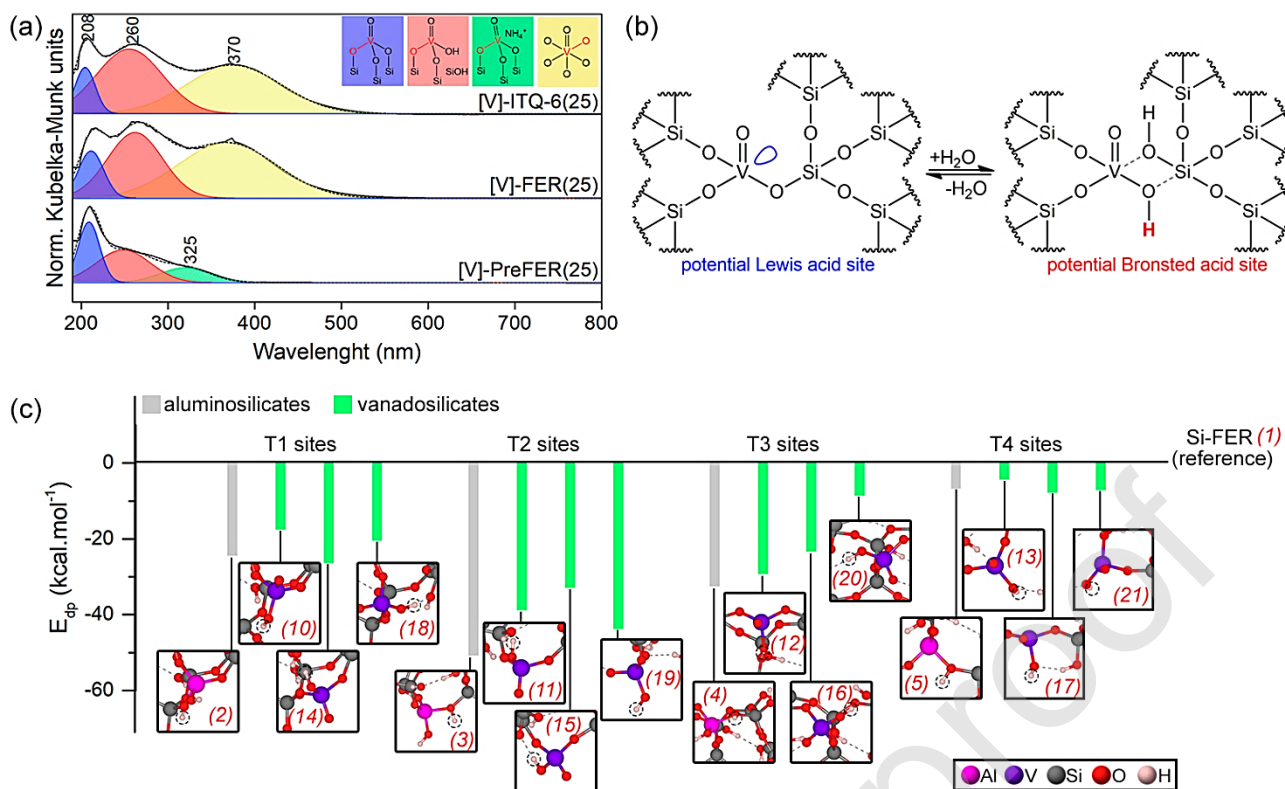


Figure 2. (a) Diffuse-reflectance UV-vis spectra of as-prepared PreFER, FER, and ITQ-6 materials. (b) Proposed conversion of Lewis acid sites into extrinsic Brønsted acid sites by dissociative adsorption of water on vanadosilicates. (c) Calculated deprotonation energy (E_{dp}) over Al and V sites of ferrierite layer in different T sites. Deprotonation energies of hydroxyl groups of siliceous structure in different T sites were used as reference (Table S2). The dashed black circle represents the proton removed from the structure. Red numbers in parenthesis are referent to calculated structure configurations in Figure S6.

The formation of a hydroxylated group (V-OH) is commonly attributed to dissociative adsorption of water on a vanadium site[48], as depicted in Figure 2b. Potential Lewis sites on empty d orbitals of vanadium allow the adsorption and dissociation of water to generate potential Brønsted acid sites[49]. Some works suggest that their formation is favored even at room temperature under humid conditions[26,48], which explains the observation of a related band on spectra, and they are reversible under dry conditions (high-temperature pre-treatments and/or vacuum), as observed by low acidity measurements by NH_3 and pyridine chemisorption (Figure S5). Due to low vanadium content, it is quite challenging to obtain good resolution spectra to determine the Brønsted acid character of these sites by FTIR using pyridine as probe molecule without further pre-treatment and by using a non-evacuated cell. By knowing this, and since it is not possible to measure the deprotonation energy of

catalysts[50], the acidity of vanadosilicates was estimated by density functional theory (DFT) calculations of deprotonation energies and compared to that calculated by Al-containing FER structure zeolites presenting intrinsic Brønsted acidity. This type of material is activity on dehydration step of glycerol to produce acrolein under oxidative conditions as previously reported[51]. DFT calculations were focused on the FER structure layer (Figure S6a) with T2 sites in terminal positions, not considering proton stabilization effects[52] by oxygens of the 8 and 10-membered rings, a model that well represents the layered ITQ-6 material. Optimized structures of the siliceous form (Figure S6b), Al-substituted (Figure S6c) and V-substituted (Figures S6d) materials on different T sites were considered. The deprotonation energy of hydroxyl groups on vanadosilicates generated by water dissociation on different Si-O-V of T sites (Figure S6e) and for aluminosilicates are shown in Figure 2c. Since an increase in acidity is related to the ease of removing the proton from the structures, more acidic materials will present lower deprotonation energies. These energies are present in the figure relative to the deprotonation energies of hydroxyl groups on correspondent T sites of the pure siliceous structure (Table S6). In general, it can be noted that deprotonation energies of vanadosilicates are very close to the deprotonation of Brønsted acid sites of aluminosilicates, strongly indicating that extrinsic acid sites generated by the presence of water on our vanadosilicates are considerably stronger than silanol groups and can almost reach the intrinsic Brønsted acidity of aluminosilicates in most of the structural configurations where hydroxylated sites may be present in the materials. T2 sites presented higher acidity relative to other T sites, which can be explained by high exposure of these sites on the surface of FER layers.

On the other hand, T4 sites presented lower acidities, probably associated with high proton stabilization by nearby oxygens, since sites on this position are present more internally in the structure. Additionally to the characterization of acidity, energies for dissociative

adsorption of water (E_{ads}) and substitution of vanadium on different T sites (E_{subs}) were estimated (Table S6). The lower energies of adsorption were found to be more dependent on the Si-O-V bond angle than the bond length since a variation of bond angle 130° to 178° was observed in the structures, whereas the length varied from 0.174 nm to 0.178 nm. Following the acidity, the most favored sites for vanadium heteroatom substitution during synthesis are those located in T2 positions, with energies 1.6, 5.1 and 4.1 kcal.mol⁻¹ lower than T1, T3 and T4 sites, respectively.

The catalysts were applied to the one-step oxidative dehydration of glycerol under diverse reaction conditions and the results are shown in Figure 3a and Table S7. The reaction conditions applied in this study were determined based on our previous studies regarding vanadium-based catalysts on glycerol oxidative dehydration[23,53,54]. Acrylic acid selectivity over total products was found to be around 35% in the presence of [V]-ITQ-6(25) as catalyst and 45% when [V]-FER(25) was used, under optimized reaction conditions, which for these materials were found to be 350°C in an atmosphere composed by 34 mol% of oxygen, 64 mol% of water and 2 mol% of glycerol. Since the same active sites were identified on two types of catalysts, the difference in selectivity is probably limited by structural properties, leading us to believe that acrylic acid is preferentially formed under confined spaces of 10-membered rings of the [V]-FER(25) material. By considering the obtained C₂ and C₃ oxygenates, acrylic acid is the main product, presenting selectivities around 80%. The difference with acrylic acid total selectivity, when only C₂₋₃ products are considered, is due to the harsh oxidizing conditions required, leading to carbon loss by CO_x formation (Figure S7A), commonly related to vanadium-based catalysts in this reaction[54,55]. Another point that probably is contributing to CO_x formation is related to the dehydration step, where the formation of high quantities of coke deposited on the catalyst surface is very frequently reported [56,57], and vanadium can simultaneously catalyze complete oxidation of these

compounds [23] since no considerable carbon accumulation was identified on the spent catalysts (Figure S8) avoiding deactivation by coke in these materials. Together with acrylic acid, small amounts of acrolein, acetaldehyde, acetic acid, allyl alcohol, and propanal were identified between C₂₊ oxygenated products. Formation of acetaldehyde was previously associated with decomposition of acetol, and acetic acid to oxidation of acetaldehyde[58]. These compounds are predominant between C₂₊ oxygenated products (~60%) when pure vanadium oxide is applied as catalyst (Figure S7B), probably due to the abundance of Lewis acid sites on the surface. The absence of acetol and low formation of its derived compounds in vanadosilicates, strongly indicates that Lewis acid sites are effectively blocked by water adsorption on vanadium sites, disfavoring these reaction pathways. Even though [V]-FER(25) shows high acrylic acid selectivities, comparing 2D and 3D structures, production of acrylic acid is superior in the presence of the [V]-ITQ-6(25) catalyst in all evaluated conditions. These observations are probably justified by limited diffusion of glycerol inside the 10-membered rings of [V]-FER(25), since the molecule has a kinetic diameter of around 0.54 nm[19], which is very close to the micropore diameter of the material (0.42 - 0.54 nm).

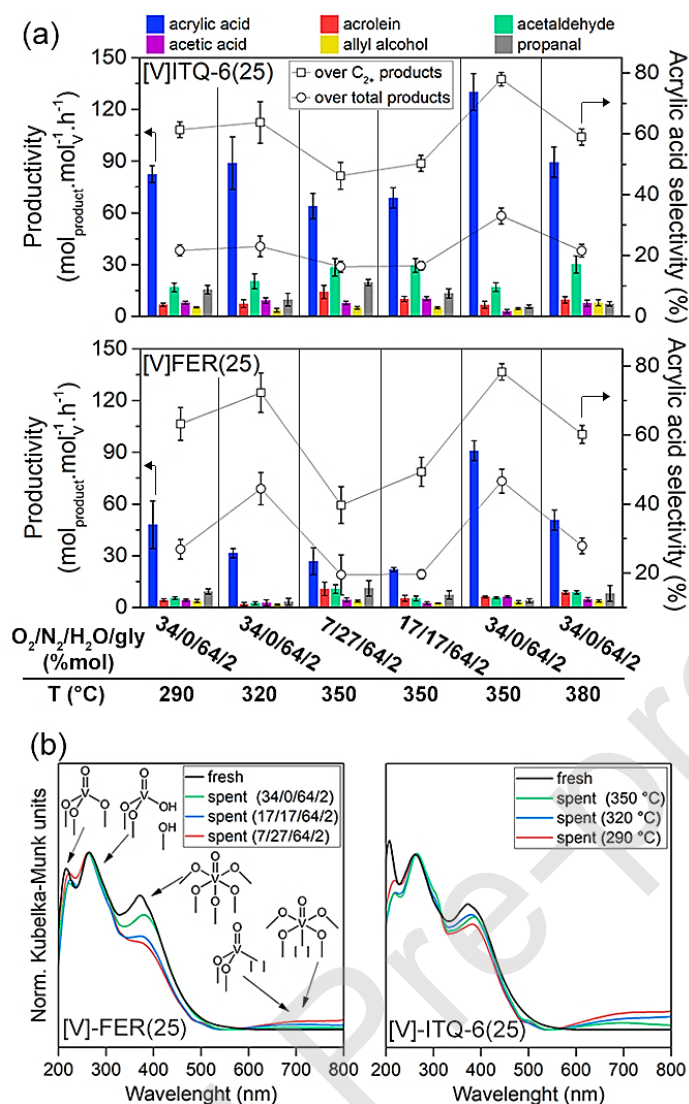


Figure 3. (a) Productivity and acrylic acid selectivity of catalysts. For each reaction condition tested, the reactor was loaded with a fresh catalyst. Average values for six aliquots collected each 1h during 6h of reaction. (b) Diffuse-reflectance UV-vis spectra of fresh and spent catalysts after 6 h of reaction at different feed compositions for [V]-Si-FER(25) and temperatures for [V]-ITQ-6(25).

After 6 h of reaction, changes in the vanadium sites of the spent catalysts relative to the fresh ones were monitored by UV-vis spectroscopy (Figure 3b). A decrease in the bands at 220 and 370 nm, related to more distorted non-hydroxylated tetrahedral and octahedral sites respectively, was observed, followed by the appearance of bands from 600 to 800 nm, related to transitions in *d-d* orbitals, characteristic for V⁴⁺ species (VO²⁺)[42]. These sites are probably involved in the step of acrolein oxidation since it is commonly reported that an equilibrium between V⁵⁺ and V⁴⁺ is formed.[53] In oxidation processes involving vanadium sites, reduction of V⁵⁺ by donating structural oxygen, and reoxidation of V⁴⁺ by molecular

oxygen, are found to occur at different rates[59], resulting in the formation of a mixed-valence structure. By observing bands at 600-800 nm it is noted that the fraction of V^{4+} in spent catalysts seems to gradually increase by decreasing temperature and the amount of oxygen on feed, which explains the better activity of catalysts over high temperatures and harsh oxidant conditions. The decrease in the area of the oxygen to vanadium (V^{5+}) CT is more pronounced than the increase in the area of the 600-800 nm region since the intensities of d-d transitions are generally about ten times lower than those of the oxygen to vanadium transitions.[42] No decrease in the area of bands related to the tetrahedral hydroxylated sites was observed, indicating that these sites are not being partially reduced to V^{4+} during the reaction, which suggests that they are not effectively active in the acrolein oxidation step. The presence of large amounts of water vapor in the reactant mixture is probably preventing the reverse transformation of these sites on non-hydroxylated tetrahedra, even at high temperatures of reaction. Combining theoretical and experimental observations of our catalytic system, a mechanism for oxidative dehydration of glycerol to acrylic acid over FER and ITQ-6 vanadosilicates is proposed in Figure 4. The activity of the glycerol dehydration step to form acrolein was attributed to tetrahedral hydroxylated sites, since the acidity of these sites was estimated by deprotonation energies to be close to the intrinsic Brønsted acidity of aluminosilicates. The formation of these sites associated with dissociative adsorption of water effectively blocked potential Lewis acid sites of vanadium and consequently the production of acetol and its derivatives. The decreasing in the area of bands related to V^{5+} non-hydroxylated tetrahedral and octahedral sites and appearance of V^{4+} bands, in the UV-vis spectra of spent catalysts, indicates the formation of a V^{4+}/V^{5+} equilibrium characteristic for a Mars van Krevelen mechanism, where metallic site is reduced by donating structural oxygen to reactant and reoxidized by molecular oxygen, and suggests that both sites are active for the acrolein oxidation step to form acrylic acid. By decreasing the mol % of O_2 in the gas feed

an increase in productivity of acrolein was noted (Figure S9). The decrease of oxygen considerable affects reoxidation of V^{4+} to V^{5+} in the second step of reaction (as observed in UV-vis spectra of spent catalysts at different feed compositions on Figure 3b), decreasing conversion of acrolein to acrylic acid. This observation supports our proposed mechanism that considers double dehydration on the first step of reaction and acrolein as intermediate of reaction.

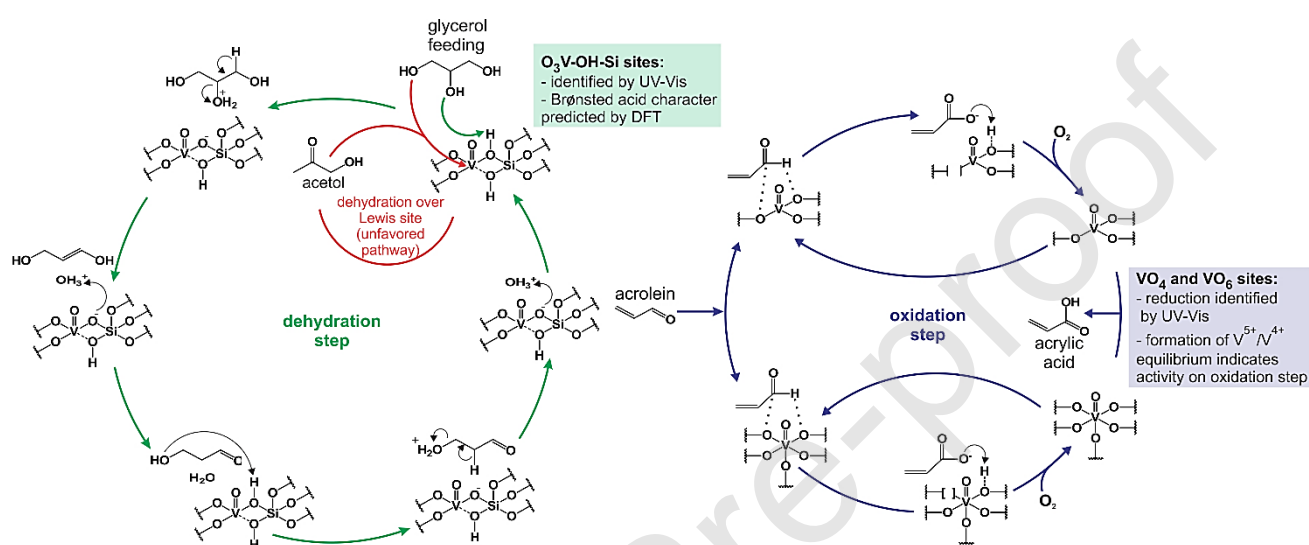


Figure 4. Proposed mechanism for glycerol oxydehydrogenation to acrylic acid over [V]-FER and [V]-ITQ-6 catalysts in a single-bed reactor. The dehydration step follows the well-established mechanism described in Figure S1, but in this case, considering the V-O-H site of lamellar vanadosilicate as the H^+ source to protonate hydroxyl groups of glycerol. The oxidation step follows a Mars van Krevelen mechanism, evidenced by the partial reduction of non-hydroxylated V sites to V^{4+} identified in UV-vis spectra.

Finally, we considered the effect of different vanadium loadings on the activity of the catalysts. [V]-FER and [V]-ITQ-6 samples with Si/V ratios of 15 and 40 in the synthesis mixture were prepared following the same procedures for [V]-FER(25) and [V]-ITQ-6(25) synthesis and characterized (Table S8 and Figure S10), leading to samples [V]-FER(15), [V]-FER(40), [V]-ITQ-6(15) and [V]-ITQ-6(40). Acrylic acid productivity ($\text{mol}_{AA} \cdot \text{mol}^{-1} \cdot \text{s}^{-1}$) reveals that as the vanadium content decreases in ITQ-6 materials, the sites become more productive, an effect not observed for FER materials, where productivity stagnates after a certain point, as in Figure 5a. Since the nature of vanadium sites present in these materials are practically the same for [V]-FER(25) and [V]-ITQ-6(25) (Figure S10ef), structural

properties are playing a more important role in the catalytic activity. Studying the condensation of the lamellar precursor into 3D FER materials during calcination in air (Figure S11), an influence of vanadium content was detected in the interaction of layers. During the calcination of PreFER a partial layer disorganization perpendicular to ($h00$) planes is observed[33], resulting in the condensation and formation of a 3D material. During the calcination of the precursor with different Si/V ratios, a decrease in the temperature interval of disorganization is noted with increasing vanadium atoms in the structure, probably associated with the increased electrostatic interaction that V sites generate in the structure. Since the final structure is the same on all FER catalysts, these observations are not relevant for catalysis on these materials, but the same effect can be expected for ITQ-6 materials. Due to the impossibility of analyzing these materials by XRD, given their structural disorganization, pore size distributions (Figure 5b) derived from physisorption isotherms and vibrations in the hydroxyl region in Fourier-transform infrared (FTIR) spectra (Figure 5c) may provide evidence of the influence of the electrostatic effect generated by the presence of vanadium on the structure of these materials. By decreasing the Si/V ratio, the occurrence of pores with diameters around 2-3 nm, related to agglomerates of closer layers, gradually decreased and broad pore distributions around 10-30 nm, related to spaces between agglomerates, shifted to lower values. Normalizing FTIR spectra of ITQ samples by the band related to isolated silanol groups[60], a decrease in the bands of H-bonded silanol groups[60] is observed. These results indicate that small amounts of vanadium in the structure facilitate the delamination process, leading to an increase in accessibility of active sites, which explains the considerable increase in productivity for acrylic acid. By exploring the extrinsic acidity and oxidant properties of distinct vanadium sites in the structure and under the optimized reaction conditions, our best catalysts, [V]-ITQ-6(40) and [V]-FER(25), exhibit total acrylic acid selectivities of 34% and 46%, acrylic acid selectivities over C_{2+} compounds of 76% and 78%,

and productivities of acrylic acid around 1.09 and 1.00 $\text{g}_{\text{acrylic acid}} \cdot \text{g}_{\text{catalyst}}^{-1} \cdot \text{h}^{-1}$, respectively, presenting no significant deactivation after 6 h on stream (Figure S12A), as observed in commercial ZSM-5 zeolite (Si/Al=15) (Figure S12B), which is mainly related to carbon deposition. These results outperform most of the zeolite-based catalysts (Table S9) that combines intrinsic Brønsted acid sites generated by the presence of aluminum in the structure for the dehydration step and vanadium for the oxidation step, in single-bed and double stacked-beds systems. The presence of multiple elements in catalysts in single-bed experiments considerably increases side reactions decreasing selectivity of acrylic acid over C_{2+} products, in most part due to intrinsic acidity on dehydration step, where part of acrolein is not oxidized to acrylic acid. Considering double stacked-beds systems under optimized conditions, this problem is solved and acrylic acid selectivity over C_{2+} oxygenate products can reach 82%, but under low WHSV values, leading to poor productivities. In this context, the presence of extrinsic acidity and oxidative character of vanadium sites in our vanadosilicate materials, single-bed experiments are comparable in acrylic acid selectivity over condensed products (C_{2+} oxygenates) to double-bed systems previously reported[61], working in higher WHSV values.

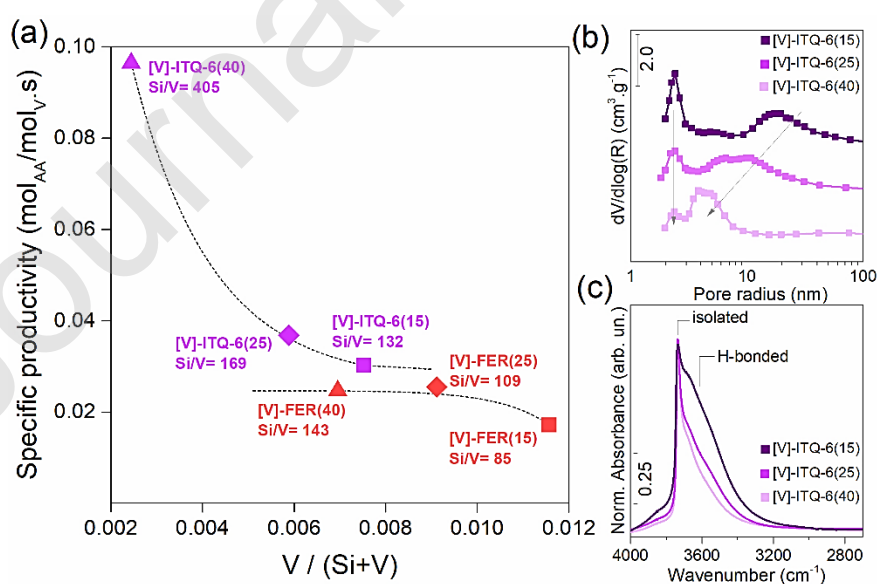


Figure 5. (a) Specific productivity ($\text{mol}_{\text{acrylic acid}}/\text{mol}_{\text{V sites}} \cdot \text{s}$) of [V]-FER and [V]-ITQ-6 catalysts at different Si/V ratios. (b) The pore size distribution of [V]-ITQ-6 catalysts at different Si/V ratios. (c) FTIR of dehydrated [V]-ITQ-6 at different Si/V ratios. Samples were heated *in situ* up to 400°C and cooled to 25°C to collect spectra.

CONCLUSIONS

We observed that Al-free vanadosilicates with analogous structures of ferrierite and ITQ-6 zeolites are active to directly catalyze oxidative dehydration of glycerol to acrylic acid. Hydroxylated vanadium sites formed under humid conditions by dissociative adsorption of water were found to generate extrinsic acidity on these materials, responsible for the glycerol dehydration step. Density functional theory calculations suggest that this acidity is comparable to the intrinsic Brønsted acidity of Al-containing zeolites of the same structure, which explains the excellent selectivity for acrylic acid. The 3D FER materials were more selective to C₂₊ products, reaching an acrylic acid selectivity of around 46% over total products but suffering from limited diffusion through 10-membered pores, considerably decreasing productivity of sites per time. The accessibility generated on 2D ITQ-6 materials considerably increased the acrylic acid productivity of the active sites. By decreasing the vanadium content, the delamination process becomes more effective, exposing more surface area and consequently access to vanadium sites. By identifying different types of sites and assigning their hypothesized functionality in each step, this work shows the possibility to apply vanadosilicates in an important reaction that combines dehydration and oxidation/reduction steps.

CRedit author statement

L.H. Vieira: Conceptualization; Investigation; Formal analysis; Writing - Original Draft. **A. Lopez-Castillo:** Software; Resources; Writing - Review & Editing. **C.W. Jones:** Supervision; Resources; Writing Review & Editing. **L. Martins:** Conceptualization; Funding acquisition; Supervision; Writing - Review & Editing.

CONFLICT OF INTEREST

The authors declare no competing financial interest.

Declaration of interests

The authors declare that they have no known competing financial interests or personal relationships that could have appeared to influence the work reported in this paper.

CRedit author statement

L.H. Vieira: Conceptualization; Investigation; Formal analysis; Writing - Original Draft. **A. Lopez-Castillo:** Software; Resources; Writing - Review & Editing. **C.W. Jones:** Supervision; Resources; Writing Review & Editing. **L. Martins:** Conceptualization; Funding acquisition; Supervision; Writing - Review & Editing.

ACKNOWLEDGMENTS

This research was supported by Sao Paulo Research Foundation, FAPESP (grants #2014/20116-6, #2017/00860-0, #2018/01258-5, #2019/12501-0, and #2019/17156-0). The authors wish to thank the Brazilian Synchrotron Light Laboratory (LNLS) in Campinas for the use of the XPD (proposal XPD-20150244) beamline. Authors also acknowledge Byung Hyun Min for TEM images and Dr. Mauro D. Acevedo for pyridine chemisorption measurements.

REFERENCES

- [1] M. Guo, W. Song, J. Buhain, *Renew. Sustain. Energy Rev.* 42 (2015) 712-725.
- [2] G. Baskar, R. Aiswarya, *Renew. Sustain. Energy Rev.* 57 (2016) 496-504.
- [3] G.M. Lari, G. Pastore, M. Haus, Y. Ding, S. Papadokonstantakis, C. Mondelli, J. Pérez-Ramírez, *Energy Environ. Sci.* 11 (2018) 1012-1029.
- [4] R. Beerthuis, G. Rothenberg, N.R. Shiju, *Green Chem.* 17 (2015) 1341-1361.
- [5] S. Ishikawa, Y. Yamada, C. Qiu, Y. Kawahara, N. Hiyoshi, A. Yoshida, W. Ueda, *Chem. Mater.* 31 (2019) 1408-1417.
- [6] X. Li, Y. Zhang, *ACS Catal.* 6 (2016) 143-150.
- [7] B. Yan, L.-Z. Tao, A. Mahmood, Y. Liang, B.-Q. Xu, *ACS Catal.* 7 (2017) 538-550.
- [8] M. Shen, Y.G. Zheng, Y.C. Shen, *Process Biochem.* 44 (2009) 781-785.
- [9] X. Li, Y. Zhang, *ACS Catal.* 6 (2016) 2785-2791.
- [10] B. Katryniok, S. Paul, F. Dumeignil, *ACS Catal.* 3 (2013) 1819-1834.

- [11] G. Landi, L. Lisi, G. Russo, *J. Mol. Catal. A Chem.* 239 (2005) 172-179.
- [12] J. Tichý, *Appl. Catal. A Gen.* 157 (1997) 363-385.
- [13] T. V. Andrushkevich, *Catal. Rev.* 35 (1993) 213-259.
- [14] G.Y. Popova, T. V. Andrushkevich, G.A. Zenkovets, L.M. Plyasova, N. V. Grebenyuk, *React. Kinet. Catal. Lett.* 41 (1990) 21-25.
- [15] P. Mars, D.W. van Krevelen, *Chem. Eng. Sci.* 3 (1954) 41-59.
- [16] G.S. Foo, D. Wei, D.S. Sholl, C. Sievers, *ACS Catal.* 4 (2014) 3180-3192.
- [17] E. Tsukuda, S. Sato, R. Takahashi, T. Sodesawa, *Catal. Commun.* 8 (2007) 1349-1353.
- [18] Y.T. Kim, K.D. Jung, E.D. Park, *Appl. Catal. A Gen.* 393 (2011) 275-287.
- [19] L.H. Vieira, K.T.G. Carvalho, E.A. Urquieta-González, S.H. Pulcinelli, C. V. Santilli, L. Martins, *J. Mol. Catal. A Chem.* 422 (2016) 148-157.
- [20] J. Deleplanque, J.L. Dubois, J.F. Devaux, W. Ueda, *Catal. Today* 157 (2010) 351-358.
- [21] C.S. Carriço, F.T. Cruz, M.B. Dos Santos, D.S. Oliveira, H.O. Pastore, H.M.C. Andrade, A.J.S. Mascarenhas, *J. Catal.* 334 (2016) 34-41.
- [22] A. Chierogato, M.D. Soriano, E. García González, G. Puglia, F. Basile, P. Concepción, C. Bandinelli, J.M. López Nieto, F. Cavani, *ChemSusChem* 8 (2015) 398-406.
- [23] L.G. Possato, W.H. Cassinelli, T. Garetto, S.H. Pulcinelli, C. V. Santilli, L. Martins, *Appl. Catal. A Gen.* 492 (2015) 243-251.
- [24] L. Liu, B. Wang, Y. Du, Z. Zhong, A. Borgna, *Appl. Catal. B Environ.* 174-175 (2015) 1-12.
- [25] M. Shamzhy, M. Opanasenko, P. Concepción, A. Martínez, *Chem. Soc. Rev.* 48 (2019) 1095-1149.
- [26] S.B. Rasmussen, R. Portela, P. Bazin, P. Ávila, M.A. Bañares, M. Daturi, *Appl. Catal. B Environ.* 224 (2018) 109-115.
- [27] B. Dou, V. Dupont, P.T. Williams, H. Chen, Y. Ding, *Bioresour. Technol.* 100 (2009) 2613-2620.
- [28] C. Lee, W. Yang, R.G. Parr, *Phys. Rev. B* 37 (1988) 785-789.
- [29] A. Schäfer, C. Huber, R. Ahlrichs, *J. Chem. Phys.* 100 (1994) 5829-5835.
- [30] R. Ahlrichs, M. Bär, M. Häser, H. Horn, C. Kölmel, *Chem. Phys. Lett.* 162 (1989) 165-169.
- [31] L.R. Borges, A. Lopez-Castillo, D.M. Meira, J.M.R. Gallo, D. Zanchet, J.M.C. Bueno, *ChemCatChem* 11 (2019) 3064-3074.
- [32] International Zeolite Association Web Page, <https://europe.iza-structure.org/IZA-SC/framework.php?STC=FER>.
- [33] L. Schreyeck, P. Caullet, J.C. Mougènel, J.L. Guth, B. Marler, *Microporous Mater.* 6 (1996) 259-271.
- [34] P.A. Vaughan, *Acta Crystallogr.* 21 (1966) 983-990.
- [35] A. Corma, U. Diaz, M.E. Domine, V. Fornés, *Angew. Chemie - Int. Ed.* 39 (2000) 1499-1501.
- [36] P. Schneider, *Appl. Catal. A, Gen.* 129 (1995) 157-165.
- [37] G. Chen, H. Liu, *Environ. Sci. Technol.* 51 (2017) 11643-11651.
- [38] H. Kosslick, V.A. Tuan, R. Fricke, C. Peuker, W. Pilz, W. Storek, *J. Phys. Chem.* 97 (1993)

5678-5684.

- [39] Z. Kang, X. Zhang, H. Liu, J. Qiu, K.L. Yeung, *Chem. Eng. J.* 218 (2013) 425-432.
- [40] T. Blasco, M.A. Cambor, A. Corma, J. Pérez-Pariente, *J. Am. Chem. Soc.* 115 (1993) 11806-11813.
- [41] R. Bulánek, L. Čapek, M. Setnička, P. Čičmanec, *J. Phys. Chem. C* 115 (2011) 12430-12438.
- [42] G. Busca, L. Marchetti, G. Centi, F. Trifiro, *Langmuir* 2 (1986) 568-577.
- [43] G.L. Paz, E.C.O. Munsignatti, H.O. Pastore, *J. Mol. Catal. A Chem.* 422 (2016) 43-50.
- [44] M.K. de Pietre, F.A. Bonk, C. Rettori, F.A. Garcia, H.O. Pastore, *Microporous Mesoporous Mater.* 145 (2011) 108-117.
- [45] F. Tielens, M. Trejda, M. Ziolek, S. Dzwigaj, *Catal. Today* 139 (2008) 221-226.
- [46] Q. Wang, Y. Zhang, J. Zheng, T. Hu, C. Meng, *Microporous Mesoporous Mater.* 244 (2017) 264-277.
- [47] R. Monaci, E. Rombi, V. Solinas, A. Sorrentino, E. Santacesaria, G. Colon, *Appl. Catal. A Gen.* 214 (2001) 203-212.
- [48] A.E. Lewandowska, M. Calatayud, F. Tielens, M.A. Bañares, *J. Phys. Chem. C* 117 (2013) 25535-25544.
- [49] A. Held, J. Kowalska-Kuś, Y. Millot, F. Averseng, C. Calers, L. Valentin, S. Dzwigaj, *J. Phys. Chem. C* 122 (2018) 18570-18582.
- [50] A.J. Jones, E. Iglesia, *ACS Catal.* 5 (2015) 5741-5755.
- [51] M.B. dos Santos, H.M.C. Andrade, A.J.S. Mascarenhas, *Microporous Mesoporous Mater.* 223 (2016) 105-113.
- [52] M. Sierka, J. Sauer, *J. Phys. Chem. B* 105 (2001) 1603-1613.
- [53] A.S. Paula, L.G. Possato, D.R. Ratero, J. Contro, K. Keinan-Adamsky, R.R. Soares, G. Goobes, L. Martins, J.G. Nery, *Microporous Mesoporous Mater.* 232 (2016) 151-160.
- [54] L.F. Rasteiro, L.H. Vieira, L.G. Possato, S.H. Pulcinelli, C. V. Santilli, L. Martins, *Catal. Today* 296 (2017) 10-18.
- [55] L.F. Rasteiro, L.H. Vieira, C. V. Santilli, L. Martins, *RSC Adv.* 8 (2018) 11975-11982.
- [56] L.G. Possato, R.N. Diniz, T. Garetto, S.H. Pulcinelli, C. V. Santilli, L. Martins, *J. Catal.* 300 (2013) 102-112.
- [57] M. V. Rodrigues, C. Vignatti, T. Garetto, S.H. Pulcinelli, C. V. Santilli, L. Martins, *Appl. Catal. A Gen.* 495 (2015) 84-91.
- [58] S. Suganuma, T. Hisazumi, K. Taruya, E. Tsuji, N. Katada, *Mol. Catal.* 449 (2018) 85-92.
- [59] L.H. Vieira, L.G. Possato, T.F. Chaves, J.J. Lee, T.P. Sulmonetti, C.W. Jones, L. Martins, *ChemCatChem* 12 (2020) 141-151.
- [60] A.M. Love, C.A. Carrero, A. Chierogato, J.T. Grant, S. Conrad, R. Verel, I. Hermans, *Chem. Mater.* 28 (2016) 5495-5504.
- [61] Y.S. Yun, K.R. Lee, H. Park, T.Y. Kim, D. Yun, J.W. Han, J. Yi, *ACS Catal.* 5 (2014) 82-94.